Journal of Manufacturing Processes 120 (2024) 719–732

Contents lists available at ScienceDirect

Journal of Manufacturing Processes

journal homepage: www.elsevier.com/locate/manpro

Analysis of cutting tool geometry induced machining response, surface integrity and anisotropy relation of additively manufactured 316L stainless steel

Ozhan Kitay [a,b,*], Yusuf Kaynak [c]

[a] Department of Machine and Metal Technologies, Bilecik Seyh Edebali University, 11100 Bilecik, Türkiye
[b] Department of Mechanical Engineering, Institute of Pure and Applied Sciences, Marmara University, Goztepe Campus, Kadikoy, 34722 Istanbul, Türkiye
[c] Department of Mechanical Engineering, Faculty of Technology, Marmara University, 34854 Maltepe, Istanbul, Türkiye

ARTICLE INFO

Keywords:
Additive manufacturing
Stainless steel
Tool geometry
Anisotropy
Surface integrity
Strain rate

ABSTRACT

Although the machining responses of additively manufactured (AM) materials generally differ from wrought materials due to their microstructural properties, there is no study examining the effects of varying cutting tool rake angles in the machining of AM 316L stainless steel material. The aim of this paper is to evaluate the effects of machining using varying cutting tool rake angles and cutting speeds on the cutting response in terms of cutting force, tool wear, chip morphology and surface integrity characteristics such as microstructure, micro-hardness and x-ray diffraction (XRD) analysis of powder bed fusion – laser beam (PBF-LB) 316L. The effect of the tool rake angle on the anisotropic structure of the material was revealed by examining the machining-induced affected layer from both the built and scan planes and by comparing it with the wrought material. The findings showed that PBF-LB 316L behaves more abrasively than the wrought, creating higher cutting force and tool wear due to the differences in the friction coefficient and thermal conductivity of the materials. Although the machining-induced affected layer is not the same in the built and scan planes of the PBF-LB material due to anisotropy, it is considerably higher compared to the wrought material, especially at negative rake angles. While the hardness of PBF-LB material is higher at a low cutting speed and negative rake angle, the hardening capacity of wrought material is higher at high cutting speed and negative rake angle. PBF-LB chips have repeated adiabatic shear bands and the secondary deformation zone is more evident in wrought chips.

1. Introduction

Additive manufacturing (AM) provides an alternative to conventional manufacturing methods such as machining, and facilitates the production of complex shaped parts [1]. Also, AM technologies are becoming more preferable because they enable the production of functional near-net shape products from difficult-to-cut materials [2]. 316L stainless steel is a difficult material to cut and it is frequently used in areas such as in the aerospace and biomedical industry. In general, these parts have to be manufactured with high precision [3]. However, it is not possible to obtain the desired surface quality in the parts manufactured by the AM [4]. The AM method can deliver near a net-shaped product, but machining is still needed as a post-processing method to obtain parts with the desired tolerance and accuracy due to it not having an acceptable surface quality [5].

The microstructures of metallic parts manufactured by the AM methods are completely different compared to their wrought counterparts. PBF-LB is one of the most widely used AM methods. In the manufacturing process of AM parts, the plane directions create anisotropy in the material [6]. Currently, the amount and size of microstructure characteristics, such as melting pool, sub-grains, and columnar dendrites, vary due to the influence of the selected PBF-LB method manufacturing parameters such as laser power, scanning speed, hatch distance, etc. [7]. Modifications to one or more of these manufacturing parameters will also have an impact on the product's mechanical, anisotropic, and fatigue characteristics. It is possible to create every product with the same quality by figuring out the optimum PBF-LB process parameters, thanks to online [8] and offline [9] quality control processes in addition to operator control. Thus, products with predictable properties can be manufactured. However, unpredictable

* Corresponding author.
E-mail address: ozhan.kitay@bilecik.edu.tr (O. Kitay).

https://doi.org/10.1016/j.jmapro.2024.04.054
Received 25 January 2024; Received in revised form 20 March 2024; Accepted 20 April 2024
Available online 3 May 2024

failure situations may still occur due to errors such as uneven delivery of the powder material layer, deviations in optimal process parameters caused by changes in the laser beam, the effect of optical components and scanning system, metallurgical pores, and high internal stresses in parts due to the high temperature changes.

Although the working principle of machining is simple, it often consists of unpredictable dynamics that will directly affect the properties of the workpiece. During machining, uncontrollable dynamics such as chip wrapping, tool-workpiece friction, tool wear, machine rigidity, and thermomechanical effects influence the surface integrity characteristics and final performance of the machined part [10]. When all these factors are considered together, it is obvious that changes in the surface integrity characteristics of PBF-LB parts after machining as post-processing will be highly complex and crucial to final product performance. This is because machining results are predictable for the equiaxed grain wrought 316L. However, it is unclear whether the optimum machining parameters for wrought material are also suitable for PBF-LB 316L with anisotropic characteristics. Although they have the same chemical composition, the fact that PBF-LB materials have higher hardness and less ductility compared to wrought materials supports this situation [11]. Therefore, in the machining of PBF-LB 316L material, it is necessary to determine the effect of the process parameters on the changes in the surface integrity characteristics and their relationship with the deformation behavior. To understand the changes in anisotropy, it is essential to compare it with the wrought 316L.

Another perspective is the effect of defects such as dislocation density, non-metallic inclusions, and porosity in the structure of PBF-LB materials, as well as the effect of build orientation on machinability. PBF-LB process parameters determine the mechanical properties of the as-built AM material as a result of microstructural characteristics such as texture, dimension of cellular structure, grain shape, and lattice strains. While the type, size, and amount of abrasive particles affect the abrasiveness of the material, porosity defects such as gas and lack-of-fusion affect the thermal conductivity [12]. There are studies showing that cutting tool wear is affected by the presence of abrasive particles in the machining process of AM materials [13,14]. As the thermal conductivity of AM materials is affected by porosity defects, the response of the cutting temperature to this situation is different from the wrought material with relatively fewer pores and defects [15]. Therefore, evaluation of the machinability of AM materials should be carried out together with the surface integrity characteristic.

There are many studies examining the applicability of different machining strategies as post-processing to products manufactured with different AM technologies. Bruschi et al. investigated the effect of cutting parameters on cutting tool wear in the machining of AM Ti6Al4V alloy. They observed that greater abrasive wear and oxide scales were formed compared to wrought machining [16]. Sartori et al. investigated tool flank and crater wear during machining of AM Ti64 alloy. It has been observed that less flank wear occurs on the cutting tool while machining wrought material [17]. Dang et al. compared the drilling performance of AM Ti alloy with wrought. Less cutting force was measured for wrought. In addition, while there was a small amount of microchipping on the tool in wrought drilling, coating peeling-off occurred on the tool in AM drilling [18]. In another study, Careri et al. focused on the effect of different cutting parameters on the microstructure of AM Inconel 718 alloy and tool wear [19]. On the other hand, it is seen that the studies related to the machining of AM 316L stainless steel are mostly focused on the surface integrity characteristics and machinability capacity. Li et al. studied the typical cutting response and microstructure of AM 316L. A deeper white layer formation was observed in AM material compared to wrought at the same cutting parameters [20]. Kaynak and Kitay examined the effect of machining parameters and showed the formation of nano-sized homogeneous equiaxed grains due to plastic deformation on the machined surface of AM 316L [21]. In another study, they examined the effect of machining parameters on the microhardness of AM 316L material [22]. In the studies carried out, the effects of machining parameters and conditions on surface integrity characteristics and machining responses were examined in machining studies generally applied to difficult-to-cut materials manufactured with AM [23–25]. It is seen that only Ti-based AM materials have been examined in detail for cutting tool wear. However, there is no study examining the effects of cutting tool geometry on the surface integrity characteristics, anisotropic behavior, and cutting response of AM materials.

The aim of this study is to perform the machining process of PBF-LB 316L stainless steel material at different cutting tool rake angles, and also to determine the optimum cutting parameters by comparing with the wrought, taking into account the anisotropic and deformation behaviors in terms of cutting response and surface integrity characteristics. The cutting response was evaluated experimentally by means of cutting force and chip morphology. The effect of tool geometry and cutting speed on machined material surface integrity was also examined by comparing it with wrought material.

2. Experimental setup

The materials used in this study are powder bed fusion – laser beam (PBF-LB) manufactured and wrought 316L stainless steel with a diameter of 25 mm and a length of 60 mm. As shown in Fig. 1, the materials were formed into 4 mm thick discs from both sides for the orthogonal cutting experiments. The as-built hardness of PBF-LB 316L is 240 ± 10 HV and as-receive hardness of wrought 316L is 245 ± 10 HV.

The machining experiments were performed on a Doosan Puma GT2100 CNC turning center. The cutting tools used in experiments were Sandvik TCMW 16 T308 H13A without any coating and with 25 μm edge radius. The tool has a neutral rake angle and a clearance angle of 7°. The discs were turned orthogonally until the diameter decreased from 25 mm to 15 mm, and the total length of cut is 6283 mm. A new cutting tool was used in each experiment. Tool images were taken when the 15 mm diameter was reached in the cutting process. STNCN 2525 M16 ($\gamma = -6°, -3°, 0°, +3°, +6°$) tool holders were specially produced for five different rake angles and used in the tests. Cutting tests were carried out under dry conditions without any coolant or lubricant. Cutting speeds were chosen as 7.5, 30 and 120 m/min and uncut chip thickness was chosen constant as 0.05 mm. Cutting forces were measured using the Kistler 2129AA dynamometer. Cutting temperature during experiments was measured via Optris PI400 infrared camera with an emissivity of 0.6 according to the catalog. All process parameters are listed in Table 1.

For surface integrity analysis, specimens were cut from the machined samples with a precision cutting device. Due to their anisotropic microstructure, PBF-LB specimens were cold-mounted from both built and scan planes, and wrought specimens were cold-molded from a single plane due to its equiaxed microstructure. The schematic representation of the cold-mounted specimens and the as-built microstructure image of the PBF-LB material are shown in Fig. 2. Also, PBF-LB and wrought chips were cold-mounted. Specimens molded with acrylic solution were polished with conventional techniques. Polished specimens were etched with 16.7 vol% HNO_3 + 33.3 vol% Glycerol +50 vol% HCl solution and their microstructures and machining-induced layers were examined under Keyence VHX6000 digital microscope. The microscope was also used to take cutting tool images and measure the chip thicknesses. Vickers microhardness values were measured with Future-Tech FM310e device following ASTM E 384 standard. Microhardness of each specimen was determined by an average of 10 measurements. X-ray diffraction (XRD) measurements were performed by a Malvern Panalytical device with CuKa radiation ($\lambda = 1.54060$ Å) and scan speed of 15° /min.

3. Results and discussion

3.1. Cutting forces

Cutting forces are one of the main parameters that directly affect the

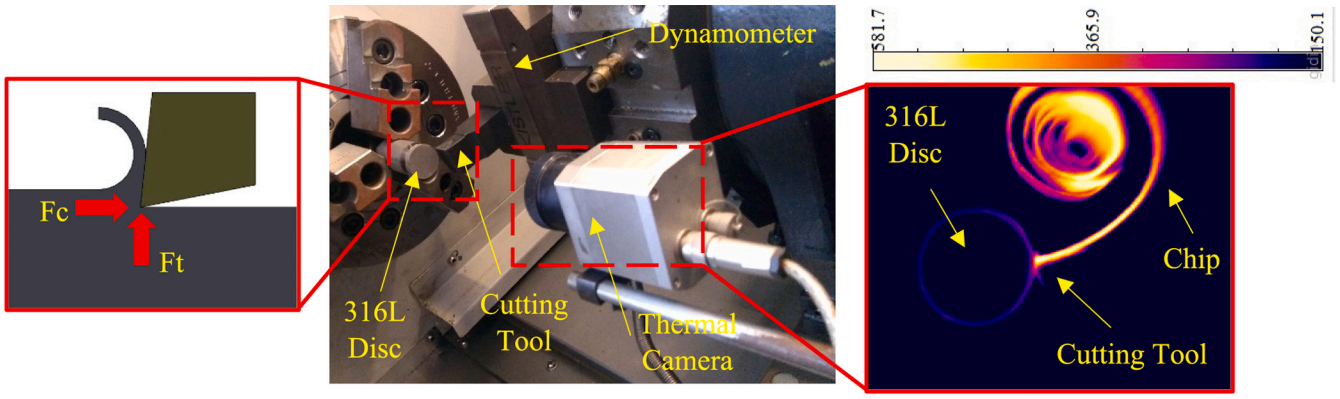

Fig. 1. Orthogonal cutting setup.

Table 1
LPBF and cutting experiment parameters.

PBF-LB parameters	Value	Machining Parameters	Value
Laser Power (W)	195	Materials	LPBF, Wrought
Laser Scan Speed (mm/s)	1083	Cutting Speed, Vc (m/min)	7.5, 30, 120
Hatch distance (μm)	90	Uncut Chip Thickness, t_0 (mm)	0.05
Layer thickness (μm)	20	Rake Angle, γ (°)	−6, −3, 0, 3, 6
Scanning strategy	67° bidirectional	Machining Condition	Dry

surface integrity of the machined material. Moreover, cutting forces can be affected by factors such as tool-chip friction, tool geometry, and tool or workpiece material [26]. The cutting forces measured in the experiments of cutting PBF-LB discs at various tool rake angles are shown in Fig. 3a, and thrust forces are shown in Fig. 3b. While the forces were high at low cutting speed, there was a decrease in cutting forces due to the increase in cutting speed. The increase in temperature due to the increased cutting speed creates a thermal effect in the cutting zone. This reduces the energy required for plastic deformation. Another trend is related to the rake angle. The cutting forces decrease from negative to a positive rake angle at each cutting speed value. Also, error bars are usually larger at negative rake angle values. Tool rake angle is a factor that directly affects the shear angle formed in the shear plane. The low rake angle provides a small shear angle. Thus, it creates a larger shear plane area and cutting force. The change in cutting force from −6° to °6 rake angle is 40 %, 51 % and 36 % at cutting speeds of 7.5, 30 and 120 m/min, respectively. Thrust force on the other hand, is an indicator that represents the load on the cutting tool. Abrasions, plastic deformations, and fractures in the cutting tool can directly affect the measured force. Therefore, cutting tool performance can be analyzed with thrust force in orthogonal cutting operations. In general, the highest thrust force values were measured at negative rake angles at all cutting speeds. In that case,

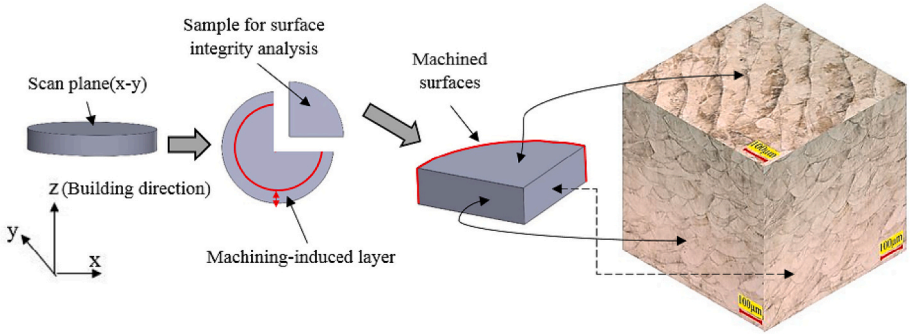

Fig. 2. Presentation of the specimen for surface integrity analysis and as-built microstructure image.

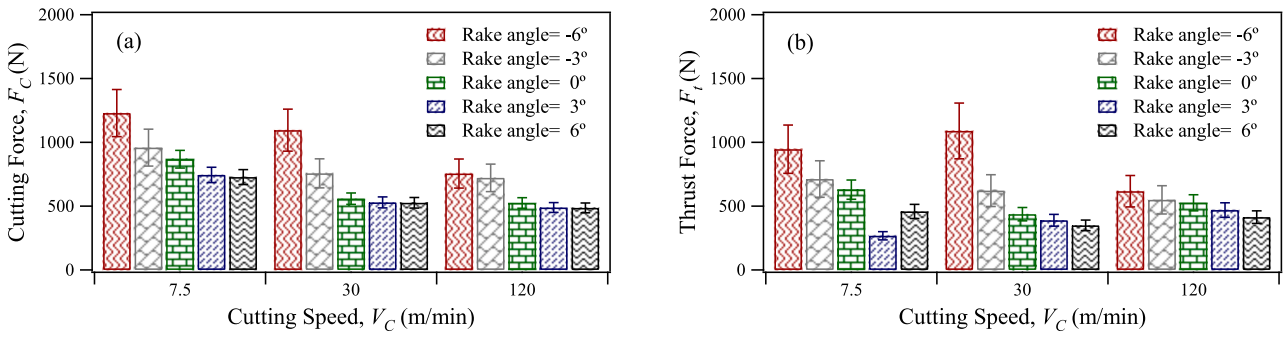

Fig. 3. Measured a)cutting and b)thrust forces at various tool rake angles and cutting speeds.

it is possible for the cutting tools at a negative rake angle to occur in situations such as wear and fracture. A detailed analysis is made in the next section.

The comparison of the cutting forces measured in the experiments of cutting PBF-LB and wrought discs under the same parameters are shown in Fig. 4a, and the thrust forces are shown in Fig. 4b. Cutting PBF-LB discs resulted in higher cutting forces compared to wrought discs. It is understood that PBF-LB material exhibits more abrasive behavior than wrought, and the effect of material difference on cutting force emerges. In both materials, the cutting force tended to decrease as the cutting speed increased. However, the decrease in forces is not proportionally similar. The difference between the forces measured in PBF-LB material at cutting speeds of 7.5 to 120 m/min is 38 % and 33 % at rake angle of −6° and 6°, respectively. Likewise, the difference in wrought material at 7.5 and 120 m/min cutting speeds was 15 % and 7 % at a rake angle of −6° and 6°, respectively. This situation reveals that the effect of cutting tool geometry on PBF-LB material is more than wrought. In addition, a similar situation is seen in thrust forces. As the cutting speed increases, it is clear that steady-state cutting occurs in the wrought material while the volatility in PBF-LB forces is high.

Wrought austenitic 316L stainless steel is a material with a face-centered cubic structure that does not have a significant yield point. So much so, that a negligible amount of plastic deformation can occur at 2/3 of the yield point. It is the large number of active slip systems in the fcc structure that cause this semi-elastic behavior [27]. Considering the differences in microstructural properties between wrought and PBF-LB materials, this situation becomes more complex for PBF-LB materials. While it is already known that wrought and PBF-LB materials have different tensile properties, the PBF-LB material shows different anisotropic tensile properties in the scan and built planes [28]. The same situation is valid for cutting force. Because AM material has different crystallographic textures in different cutting plane directions, the cutting forces are not the same in scanned and built planes [29]. However, in orthogonal machining experiments, cutting was always done in the same plane direction. This is the basis for the difference between PBF-LB forces and wrought forces in the orthogonal method, in the cutting process perpendicular to the z direction and towards the center of the x-y plane. Therefore, it is not appropriate to evaluate anisotropy in terms of cutting responses in this study. Instead, since anisotropy is a material property, it was deemed appropriate to examine the effect of machining on anisotropy in terms of surface integrity characteristics rather than the effect of anisotropy on machining.

3.2. Tool wear and friction

The tool-chip contact area images for the cutting tools used in the cutting experiments of the PBF-LB discs at various tool rake angles and cutting speed are shown in Fig. 5. It is possible to divide the tool images into two groups as steady-state tool-chip contact as well as plastically deformed and fractured. While abrasion and diffusion behaviors are active as tool wear mechanisms in the first group, deformations due to abrasive and fatigue wear behavior are obvious in the second group, respectively. The tool-chip contact areas occurring at all rake angle values at a cutting speed of 7.5 m/min are stable. However, at negative rake angle values at 30 m/min cutting speed, it is seen that the tool-chip contact causes the physical integrity to deteriorate due to fractures. In positive rake angle values, while the effect of abrasive wear increases, there is no deformation or fracture occured. In this respect, the cutting speed of 30 m/min is defined as the critical value in terms of tool performance. At 120 m/min cutting speed, plastic deformations and fractures occurred in the tool-chip regions at all rake angle values.

The tool-chip contact area formed in the cutting experiments of PBF-LB and wrought discs are shown in Fig. 6. Although it is possible to evaluate the tool images in two groups, the cutting speed of 30 m/min still seems to be the critical value. When the tool images are examined in terms of PBF-LB and wrought, it is clear that PBF-LB specimens in general cause a more abrasive cutting operation. There are continuous contact areas without deteriorating the physical integrity of the tools at a cutting speed of 7.5 m/min. At high cutting speeds, the effect of material differences in tool wear and fractures is evident. Regardless of the rake angle, severe tool-chip contact areas, fractures, and plastic deformations are obvious in PBF-LB machining, while stable tool-chip contact areas have occurred in the wrought. In addition, tool wear is higher at negative rake angle in both PBF-LB and wrought compared to a positive rake angle.

In fact, apart from cutting parameters, another situation that causes cutting force and wear differences in tools is anisotropy due to material differences. Although the wrought material consists of equiaxed grains in longitudinal and transverse directions, the ratio of inclusions in its structure effects the abrasive behavior. PBF-LB material consists of scanning traces on the scan plane and melting pools on the built plane. The volumetric energy density as a result of PBF-LB manufacturing parameters directly affects the dislocation density as well as the shape and size of grains and dendrites in the structure. Additionally, nano-sized oxide inclusions are present as a result of the laser and shielding gas used in the process [12]. In addition to the complex microstructure of the PBF-LB material, the dislocation density causes it to have different tensile properties than the wrought material. This situation affects the abrasive behavior.

For a better understanding of tool tribology, it is useful to examine the effects of temperature and friction. In this regard, wear at the critical 30 m/min cutting speed can be taken as basis. The average cutting temperatures measured as 561 and 434 °C in the PBF-LB cutting experiments, and 486 and 408 °C in the wrought cutting experiments at −6° and 6° rake angle values, respectively. Temperatures are lower at a positive rake angle. In the orthogonal cutting method, shear strain decreases at a positive rake angle. Since this situation causes a large shear angle to occur, the shear plane area becomes smaller compared to the negative rake angle. A large shear plane area causes more heat to occur in the primary deformation zone. The secondary deformation region is the tool rake face-chip contact point and the temperature in this region is partially lower. In the temperature measurement made in this study, the temperatures detected by the thermal camera frame were measured and these temperatures are probably higher in the tool-to-chip interface. It is

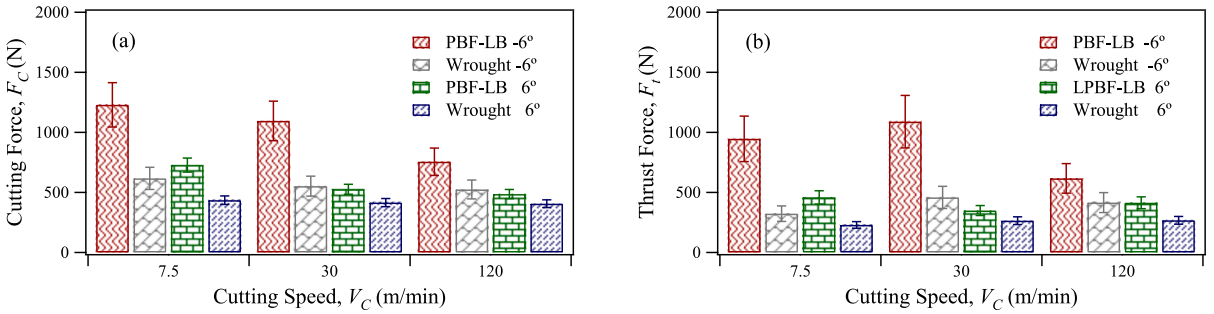

Fig. 4. Comparison of measured forces in cutting PBF-LB and wrought discs a)Cutting force and b)Thrust force.

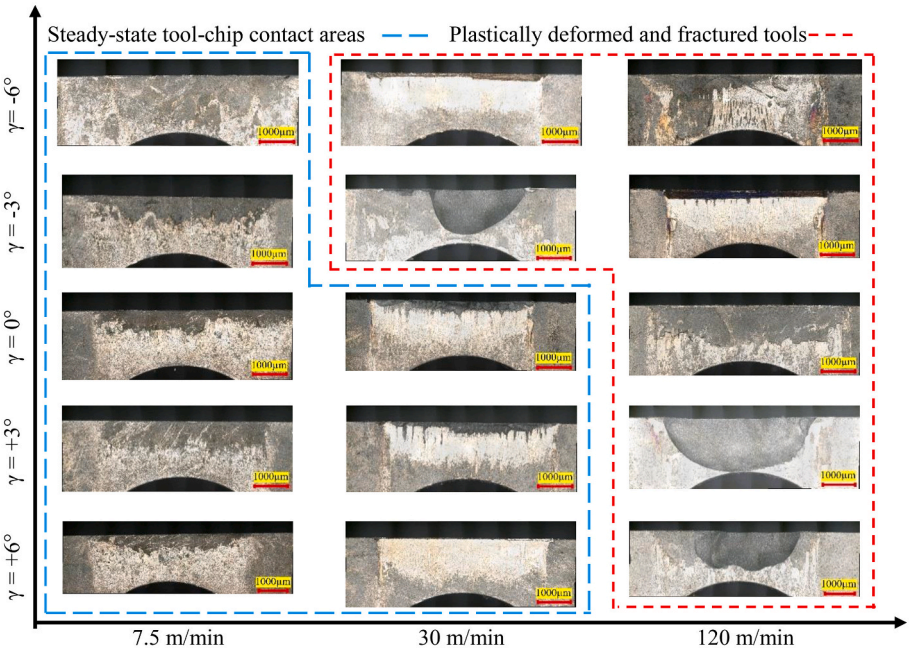

Fig. 5. Cutting tool rake surface images used in the cutting experiments of PBF-LB discs at various rake angles.

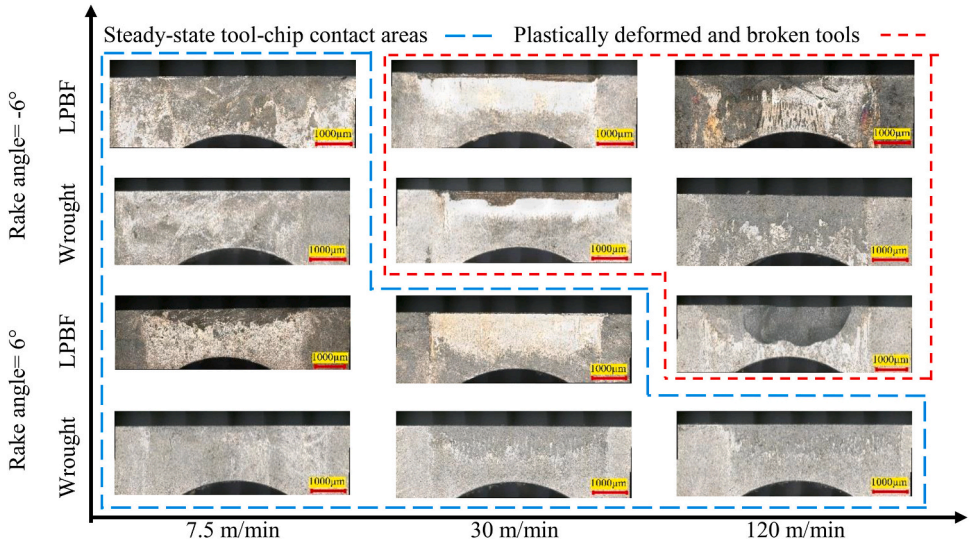

Fig. 6. Cutting tool rake surface images used in the cutting experiments of PBF-LB and wrought discs.

a known fact that the hardness of carbide cutting tools at 800 °C degrees decreases to half of their hardness at room temperature [30]. The effect of increasing temperatures on the wear resistance of any material can be explained by the wear model shown in Eq. (1).

$$W = \frac{K}{3}\frac{FL}{H} \tag{1}$$

where W is the volumetric wear of the material, K the Archard wear coefficient, F the contact force, L the cutting length, and H the hardness of the softest material [31].

Fig. 7 illustrates the development of friction during machining of PBF-LB and wrought specimens. The friction coefficient was calculated according to Eq. (2). The friction coefficient values of the PBF-LB specimens are higher than the wrought specimens. The fact that the friction coefficient values of the PBF-LB specimens are higher than the wrought specimens is a good agreement with the cutting tool wear

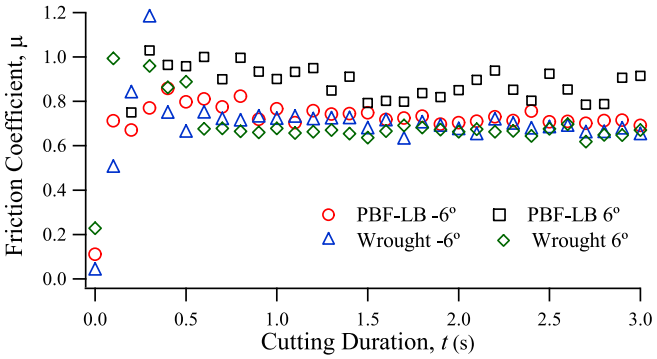

Fig. 7. Friction coefficients during machining of PBF-LB and wrought specimens (V_c = 30 m/min).

images. The average friction coefficients are 0.75 and 0.91 in the PBF-LB specimen, and 0.67 and 0.71 in the wrought specimen at −6° and 6° rake angle values, respectively.

$$\mu = \frac{F_c tan\gamma + F_t}{F_c - F_t tan\gamma} \quad (2)$$

3.3. Chip breakability and morphology

Fig. 8 shows the images of the chips formed in the cutting experiments of PBF-LB and wrought discs at various rake angle values. The effect of cutting temperature on PBF-LB chips is similar for all rake angle values. As the cutting speed increased, continuous chip form was observed. Irregular and broken chip formation occurred at a cutting speed of 7.5 m/min. The thermal effect is evident from a cutting speed of 30 m/min. Chips formed, especially at negative rake angle values, are continuous but welded to each other. Chips at a positive rake angle value are more stable. This indicates that the cutting tests at negative rake angle values are abrasive. Welded chip formation shows good agreement with the fracture and plastic deformations seen in the tool wear images presented in the previous section. All chips formed at a cutting speed of 120 m/min are similar to each other and in continuous form. It is understood from the images that the chips at a negative rake angle values are more brittle than the chips at a positive rake angle. Based on orthogonal cutting theory, rake angle can directly affect the tool-chip contact length. While the chip formed at a positive rake angle may flow away from the tool rake surface, the chip tends to curl back towards the workpiece at a negative rake angle. In this case, it causes chip formation in the fractured structure.

Wrought chips clearly reveal the material difference. This is particularly evident at a cutting speed of 7.5 m/min. PBF-LB chips are irregular and fractured while wrought chips are continuous at both rake angles of −6° and 6°. At 30 m/min cutting speed, the effect of a rake angle is similar in both materials. The chips are welded together at a negative rake angle value, while the chips are continuous in a similar structure at a positive rake angle value. The effect of material difference is seen at the cutting speed of 120 m/min. PBF-LB chips are flatter and brittle while conventional chips are relatively curly and ductile.

The microstructure images of PBF-LB chips and the measured thickness values at various rake angle values are shown in Fig. 9. Saw-toothed chip formation is observed at all rake angle values. Saw tooth structures are formed at irregular intervals but slip bands are evident. The measured chip thicknesses tend to decrease from the negative rake angle to the positive rake angle. The difference between the measured chip thickness values compared to the uncut chip thickness is higher at a negative rake angle. This difference is less at positive rake angle values. The difference between the highest measured chip thickness and the lowest measured thickness was 55 %. In orthogonal cutting, the chip thickness corresponds to the scan plane and the chip width corresponds to the built plane. In this case, chip microstructure images must contain at least scan traces as well as sub-grain and dendrite structures. Instead, there is a homogeneous chip microstructure that is far from anisotropic characteristics. The distorted melting pool and scan traces have formed dense slip bands as a result of very high dislocation density.

Wrought chip microstructure images and comparison of thickness values with PBF-LB chip are shown in Fig. 10. The effect of material differences on chip formation is obvious. While non-serrated chips were formed at 30 m/min cutting speed, serrated chip formation occurred only at negative rake angle value at 120 m/min cutting speed. This indicates that lower cutting speeds are sufficient for serrated chip formation from PBF-LB material. Serrated type chip formation may occur when difficult to cut materials are processed at high cutting speed and strain rates. As a matter of fact, serrated type chip formation is a result of temperature and strain rate. Due to the different response of the materials to the cutting process, the same type of chip formation did not occur in the same parameters. In addition, it is seen that the chip thickness of PBF-LB is higher than wrought chips and the effect of cutting parameters is similar for both materials. At 30 m/min cutting speed, there is a 43 % and 31 % difference between PBF-LB and wrought chip thicknesses at −6° and 6° rake angles, respectively.

Despite the irregular segmented structure of PBF-LB chips, distinct and repeated adiabatic shear bands can be observed. In wrought chips, deformation is more evident in the lower region corresponding to the secondary deformation region. Non-metallic inclusion types in wrought materials have a great impact on chip formation and tool life [32]. Because more ductile and lower strength NMIs can deform more easily along the primary shear plane. In this case, it facilitates chip breakability [12]. In PBF-LB material, in addition to complex microstructural characteristics, non-metallic inclusions directly affect tensile properties and strain hardening [33]. Therefore, different cutting response and chip formation are observed. Merchant theory was used as the analytical model to predict the effect of material differences from Eq. (1) to Eq. (6).

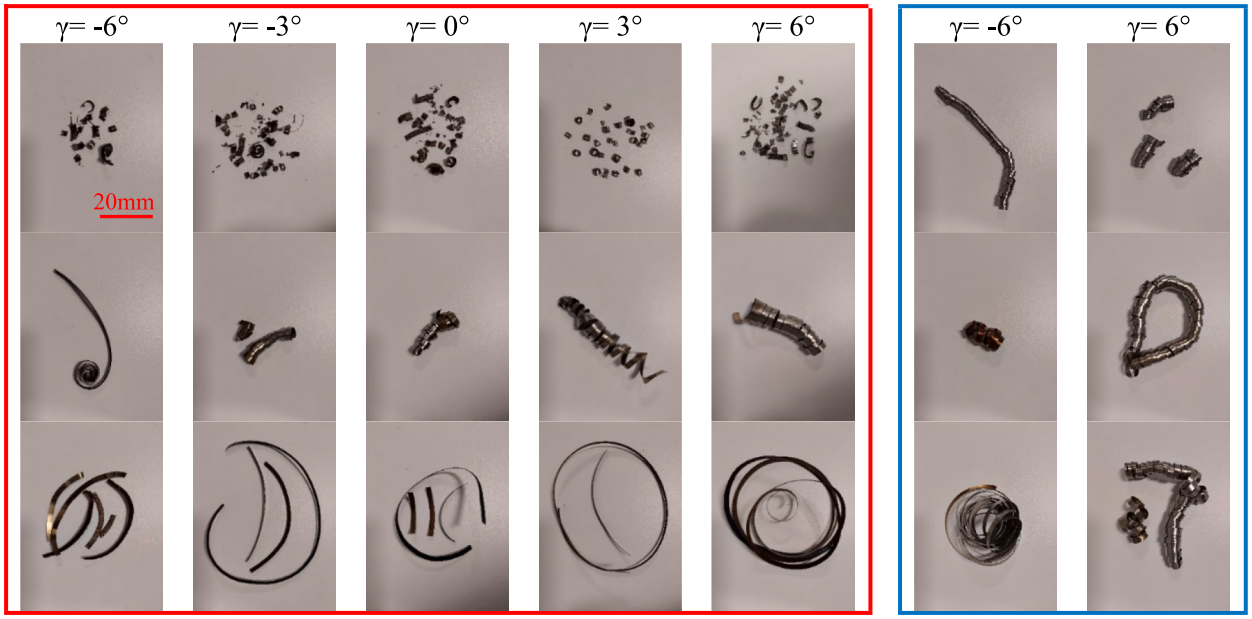

Fig. 8. Chip images of the machined specimens at various rake angles as a function of cutting speed.

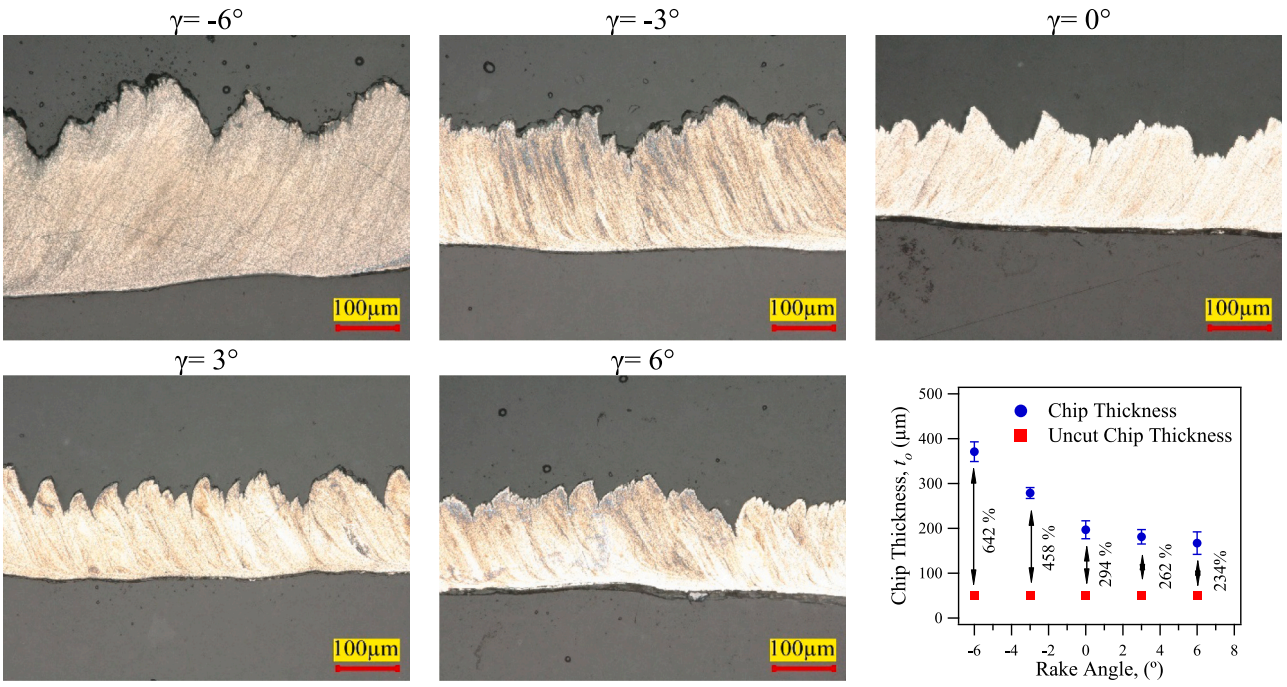

Fig. 9. Microstructure images and thickness values of the PBF-LB chips at the cutting speed of 30 m/min.

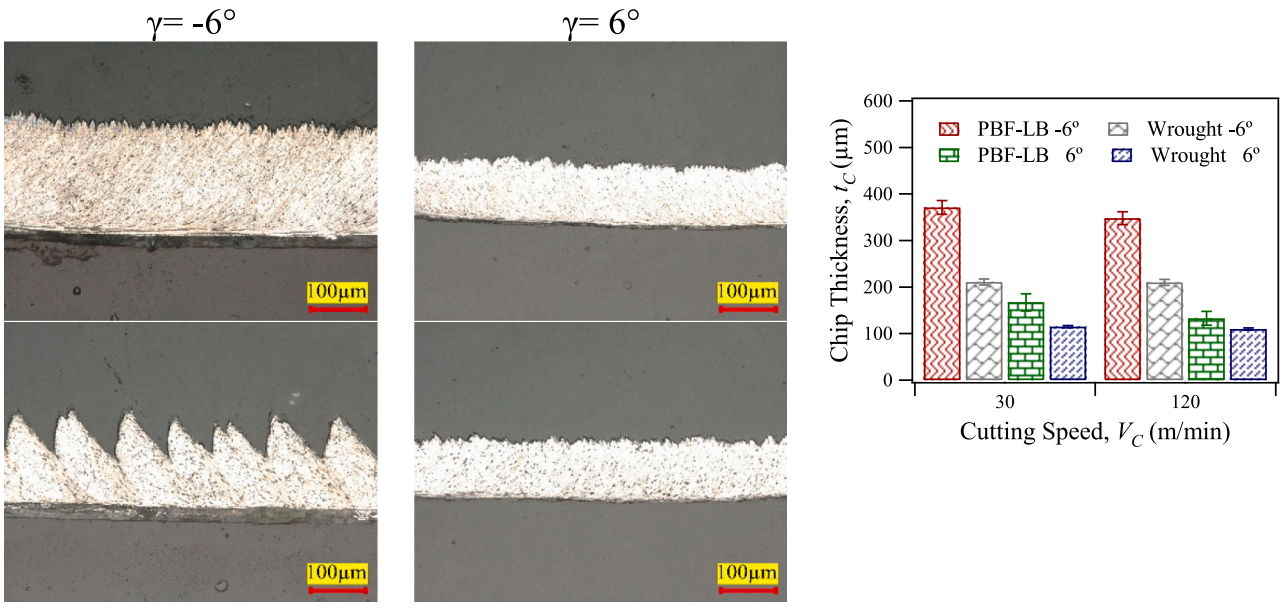

Fig. 10. Wrought chip microstructure images and chip thickness comparison with PBF-LB chip.

$$r_C = \frac{t_0}{t_C} \tag{3}$$

where r_c is the chip compression ratio, t_0 is the uncut chip thickness and t_c is the measured chip thickness.

$$\phi = tan^{-1}\left(\frac{cos\gamma}{r_C - sin\gamma}\right) \tag{4}$$

where ϕ is the shear angle and γ is the cutting tool rake angle.

$$\varepsilon = tan(\phi - \gamma) + cot\phi \tag{5}$$

where ε is the shear strain.

$$\dot{\varepsilon} = \frac{10v_C \times cos\gamma}{t_0 cos(\phi - \gamma)} \tag{6}$$

where $\dot{\varepsilon}$ is the strain rate.

Fig. 11 shows the effect of different cutting parameters and material on the calculated shear angle and strain. In Fig. 11a, there is an increase in angle values with increasing cutting speed. Thus, the phenomenon of the formation of large cutting forces as a result of small shear angle creating large shear plane area is confirmed. In Fig. 11b, there is a decrease in strain values as the cutting speed increases. As the cutting speed increases, the effect of decreasing chip thickness on strain is obvious.

The effect of different cutting parameters and material on strain rate

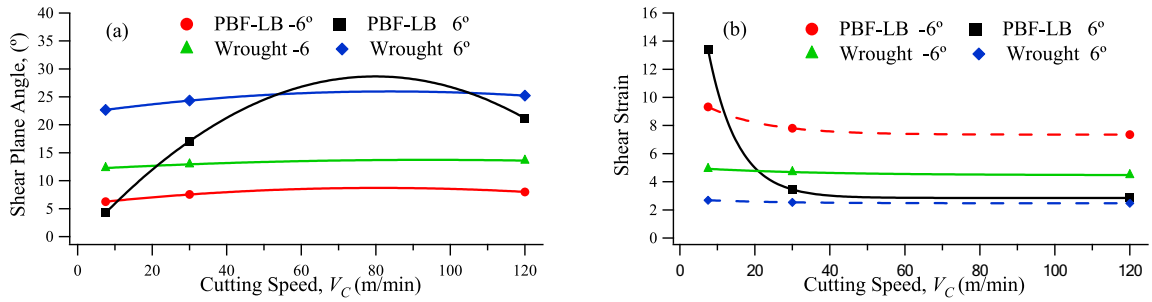

Fig. 11. Effect of cutting parameters and material on a)shear plane angle b)shear strain.

is shown in Fig. 12. As the cutting speed increased, the strain rates also increased. Wrought strain rate values at each cutting speed are higher than PBF-LB strain rate values. At cutting speeds of 7.5 and 30 m/min, the strain rates at the negative rake angle are higher for each material. However, it is the opposite for PBF-LB at a cutting speed of 120 m/min. High cutting temperature and strain rate together can cause thermal softening in materials. In other words, the difference in softening rates of materials may be due to the differences in thermal conductivity. This is because the thermal conductivity of wrought 316L is 13.31 W/m.°C [34] and the thermal conductivity of PBF-LB from the built plane is 14.3 W/m.°C [15] at room temperature. It is possible to talk about anisotropy for the thermal conductivity of PBF-LB material. In the PBF-LB material with zero porosity structure, there are negligible differences between the thermal conductivity values measured from the built and scan planes. As the amount of porosity in the structure increases, conductivity decreases in both planes, being higher in the built plane [15]. It is very difficult to achieve 100 % volumetric density ratios due to porosity defects such as gas and lack-of-fusion arising from the manufacturing method of PBF-LB materials. This situation further complicates the behavior of the material, which exhibits anisotropic thermal conductivity in the scanned and built planes. Another issue is the effect of machining as a post-processing process on reducing the porosity of PBF-LB materials [22]. As the porosity defects in the structure disappeared during machining, the thermal conductivity increased. In addition, the temperature generated during machining affects conductivity. This is because it is a known fact that the conductivity of 316L material increases at high temperatures [34]. As the temperature increases in machining, the number of free electrons and lattice vibrations increase. As a result, the kinetic energy of the atoms increases allowing thermal conductivity to increase. It is understood that the factors affecting the thermal conductivity of PBF-LB material are more complex and numerous compared to the wrought material. This is due to the fact that there are three basic factors that affect the thermal conductivity increase of PBF-LB material in the machining process: cutting temperature, porosity defects, and anisotropic characteristics. Materials with large thermal conductivity coefficients conduct heat quickly, while those with small thermal conductivity coefficients conduct heat later. It can be concluded that PBF-LB material, which has high thermal conductivity, transfers more heat to the tool during cutting compared to wrought material and causes more tool wear.

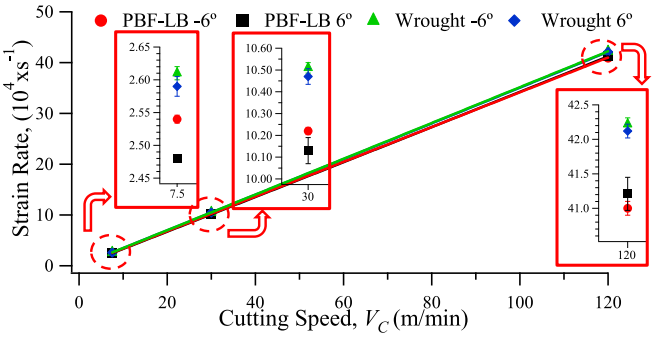

Fig. 12. Effect of cutting parameters and material on strain rate.

3.4. Microstructure

Microstructure images of PBF-LB specimens at various rake angles from both the built and scan planes and the affected layer values are shown in Fig. 13 as a function of cutting speed. The microstructure images show that the effected layer thickness is greater at a negative rake angle and lower cutting speeds. As the cutting speed increases, the affected layer of thickness decreases significantly in both the built and scan planes. At high cutting speed, the increased thermal effect dominates the mechanical effect. This causes a decrease in the force that causes plastic deformation on the material surface. Therefore, a less affected layer is formed. The least affected layers occurred at a cutting speed of 120 m/min at all rake angle values. There is no obvious difference between the affected layer thicknesses in the scan and the built plane. At the cutting speed of 30 m/min, affected layers were evident at all rake angle values. In addition, the thicknesses on the scan and built planes are similar at each rake angle. The most affected layer formation occurred at the cutting speed of 7.5 m/min. The presence of relatively lower thermal effect at low cutting speed led to the emergence of the mechanical effect required for plastic deformation. However, it is understood that the affected layer thickness in the scan and built planes is not similar and varies in all rake angle values. It is clear that PBF-LB material exhibits anisotropic behavior in scan and built planes at low cutting speed.

As-built microstructures of PBF-LB materials consist of melting pools in the built plane, and laser scanning traces in the scan plane. In addition, there are sub-grains and dendrites oriented at different angles in the details of the melting pool and scanning traces [22]. All these structures are the basis for PBF-LB materials to have anisotropic microstructure in scan and built planes. Anisotropy directly affects the usage performance of the PBF-LB product in terms of mechanics and fatigue. Particularly at some cutting speeds and rake angle values, the affected layer thickness is similar in both the scan and built planes. In this case, it is clear that the presence of similar and equal amounts of affected layers with homogeneous microstructure in both planes will have a positive effect on the performance of the PBF-LB product.

The formation of different amounts of affected layers in built and scan planes is not the sole function of microstructural anisotropy. One of the incentives that increases the effect of anisotropy is the machining process itself. PBF-LB manufacturing strategy and machining forces should be evaluated together. As can be seen in Fig. 1, the cutting force acts towards the tool rake surface and the thrust force acts towards the tool nose region. It is understood that the cutting force is parallel to the built plane formed by the melting pool structures and the thrust force is parallel to the scan plane formed by the scan traces. With the fact that cutting forces are greater than thrust forces, it is possible to talk about the existence of more mechanical forces in the built plane. Except for some exceptional cases, the fact that built plane affected layer

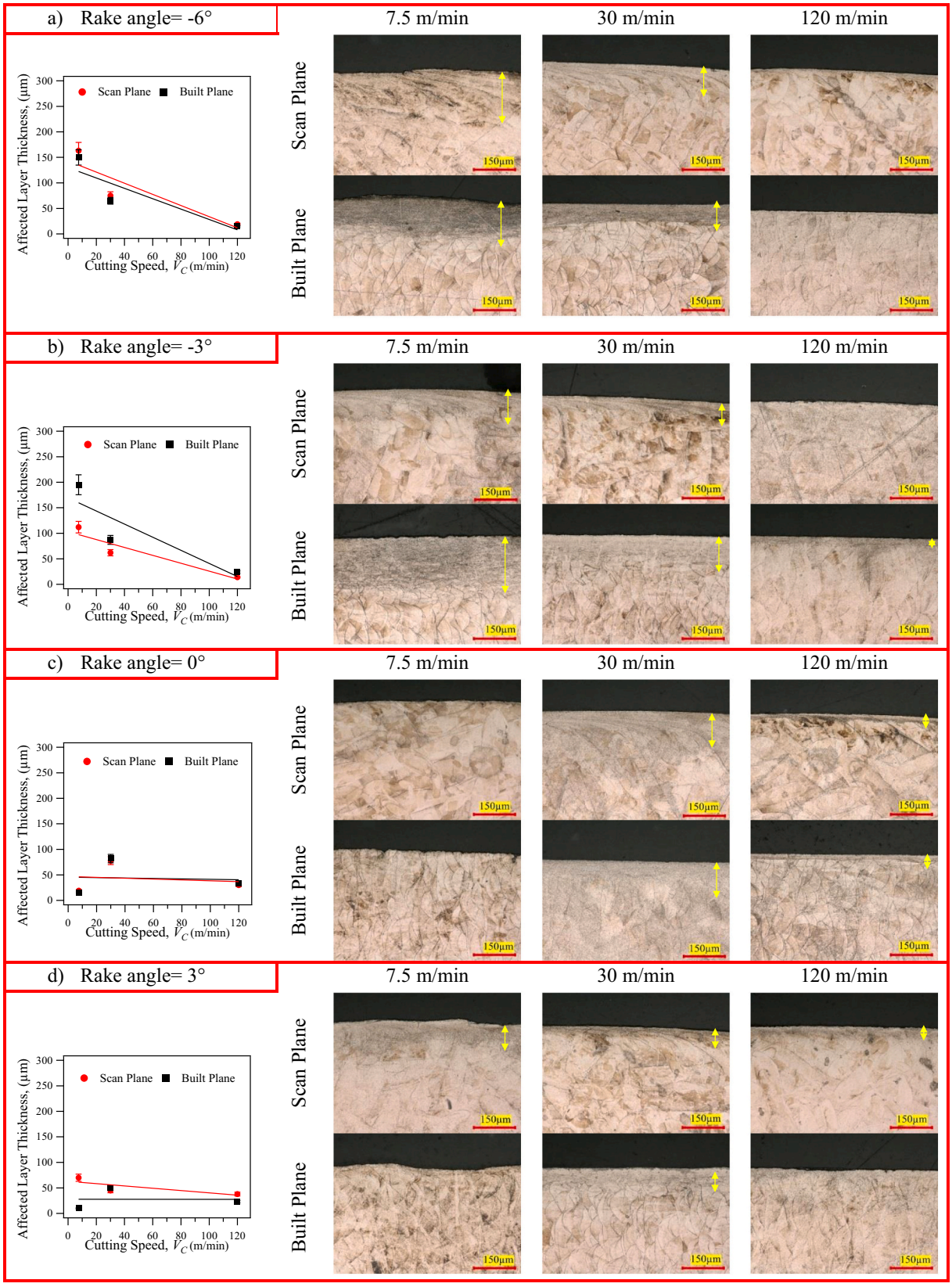

Fig. 13. Microstructure of post-processed samples and machining-induced affected layer thickness as a function of cutting speed a) $\gamma = -6°$, b) $\gamma = -3°$, c) $\gamma = 0°$, d) $\gamma = 3°$ and e) $\gamma = 6°$.

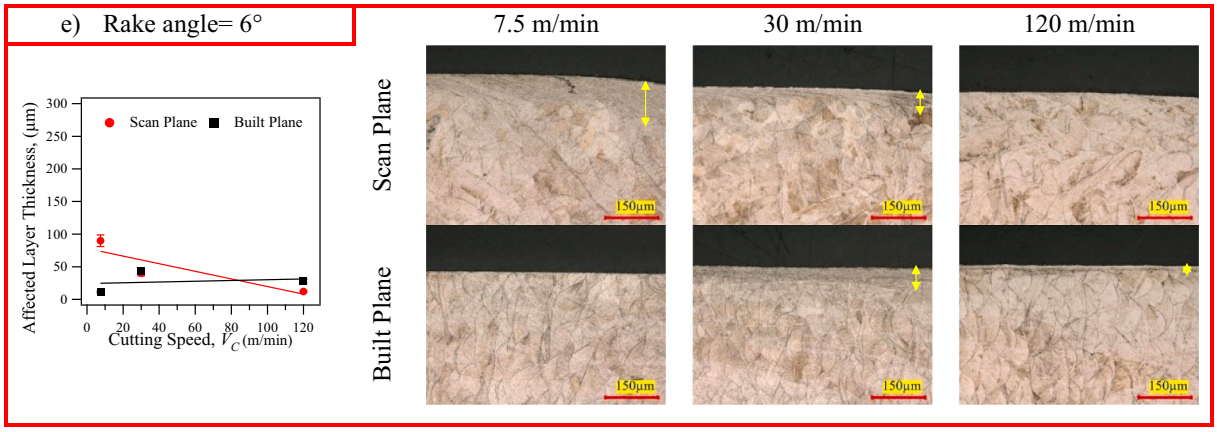

Fig. 13. (*continued*).

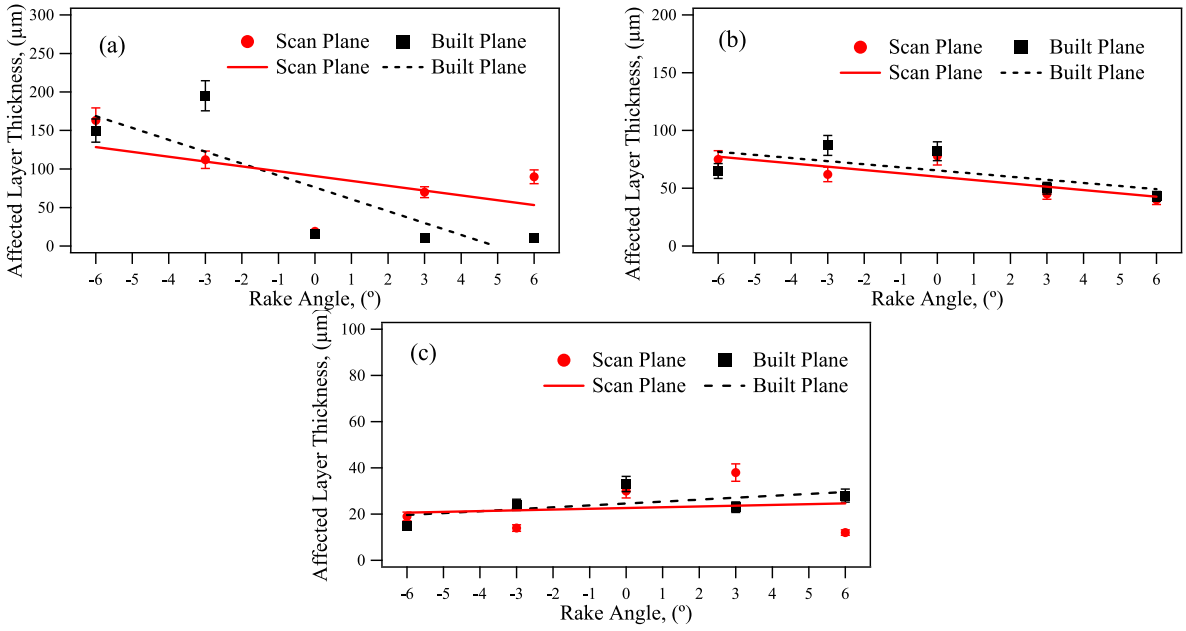

Fig. 14. Machining-induced affected layer thickness as a function of rake angle a) V_c = 7.5 m/min, b) V_c = 30 m/min c) V_c = 120 m/min.

thicknesses is greater than scan plane affected layer thicknesses supports this situation.

In Fig. 14, the affected layer thicknesses of the PBF-LB material are shown as a function of the rake angle. The scan and built plane trendlines are inconsistent in Fig. 14a while the trendlines are similar in Fig. 14b and c. This shows that anisotropy is more pronounced, although a deeper affected layer is formed at a cutting speed of 7.5 m/min. A similar situation exists for positive rake angle values at a cutting speed of 120 m/min, but the effected layer is relatively small. Another issue is that at 7.5 and 30 m/min cutting speeds, the affected layer thickness tended to decrease from negative rake angle to positive rake angle, while at 120 m/min cutting speed, an unstable situation was exhibited.

The contour plot graph of the affected layer thickness of the PBF-LB material is shown in Fig. 15a in the scan plane and in Fig. 15b in the built

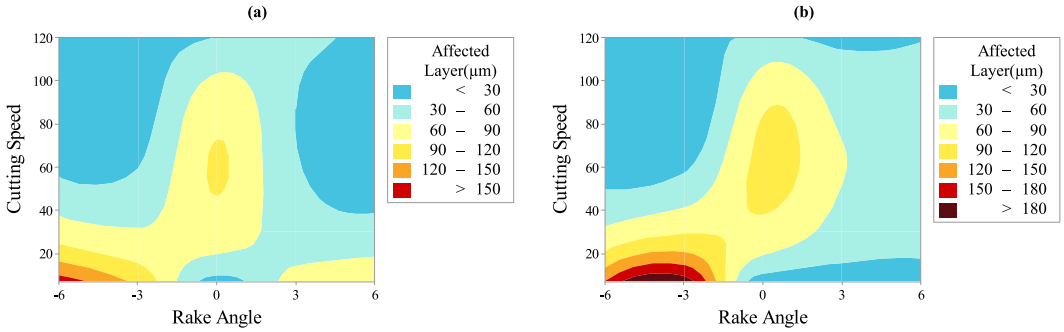

Fig. 15. Contour plot of affected layer(µm) a)Scan Plane b)Built Plane.

plane. In both planes, the affected layer thickness is highest at low cutting speed and negative rake angle. Built plane is more prominent. It is understood from the graphs that the effect of cutting speed and tool geometry has a similar effect in the scan and built planes of the PBF-LB material, but not exactly the same.

Fig. 16 shows the microstructure images of the machined wrought material and the measured affected layer thickness. It is not possible to examine the microstructure images of wrought and PBF-LB materials together. PBF-LB microstructure examination cannot be performed with the 2000× microscope magnification required for wrought material microstructure examination. This is because 500× magnification is ideal to fit the entire effected layer of the PBF-LB microstructure into the microscope frame. As a matter of fact, the highest wrought material affected layer value is at the lowest value of the PBF-LB material. In fact, this indicates a good agreement that more force is required in the experiment of cutting PBF-LB discs due to abrasive response of the material than wrought material. This is because a high force is required for a highly affected layer. The highest wrought affected layer thickness was 25 μm at a cutting speed of 7.5 m/min and a rake angle of −6°. At the same parameters, there is a difference of 85 % in the scan plane and 83 % in the built plane with the PBF-LB affected layer thickness. While the affected layer thickness of the machined wrought material may be standard in the selected cutting conditions and parameters, the same is not the case for PBF-LB. Because different selection of PBF-LB manufacturing parameters means different amount of anisotropy and mechanical properties. This may directly affect the post-process response of the PBF-LB material.

3.5. X-ray diffraction analysis

XRD patterns of as-built and PBF-LB discs machined at different rake angles are shown in Fig. 17. The main peak with (111) texture in the range of 42–45° was examined. As-built peak showed a low intensity compared with the PBF-LB peaks. PBF-LB 2 theta peak angles are different from the as-built peak angle and there are shifts in the peaks. The increase or decrease in the peak angle is due to residual stresses. In addition, the width of each peak differs from each other. According to Bragg's law as shown in Eq. (7), the peak broadening shows the decrease in grain size. These changes in peaks are a result of the thermo-mechanical effects of machining. The difference in the peaks is obvious due to the effect of the rake angle. The highest peak intensity is 237 % higher than the as-built peak intensity at the −6° rake angle value. Broadening occurred in all PBF-LB peaks compared with the as-built peak. This shows that there is grain refinement in all machined samples. It is already evident from the microstructure images. Considering the amount of shift at the peak angles, the increase in stress is the highest at −3° rake angle, while it is the least at 0° rake angle compared to as-built.

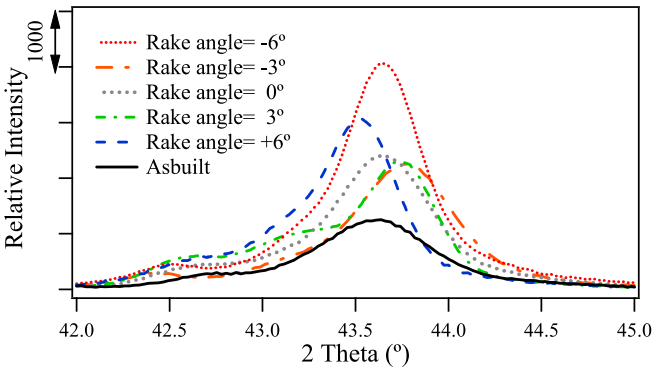

Fig. 17. X-ray diffraction patterns of main austenite peaks (V_c = 7.5 m/min).

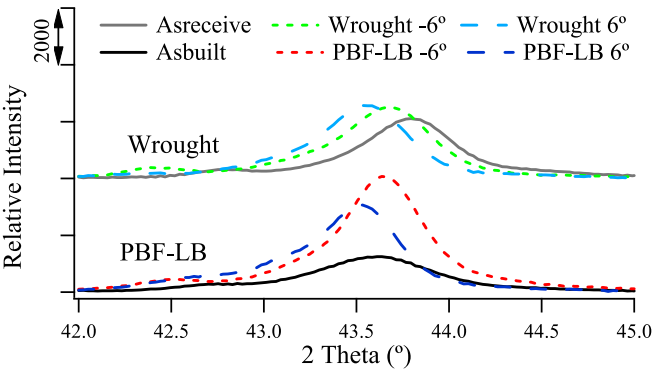

Fig. 18. XRD pattern of the as-built, as-receive, wrought and PBF-LB specimens (V_c = 7.5 m/min).

$$n\lambda = 2dsin\theta \quad (7)$$

Comparison of the XRD patterns of wrought and PBF-LB discs machined at various rake angles are shown in Fig. 18. As with PBF-LB peaks, the intensity and width of the wrought peaks are higher than as-receive. Also, the shift in the peak angles is obvious. Since the as-built and as-receive peak values are different, it would not be correct to evaluate the wrought and PBF-LB peaks together. Rather than comparing peaks, it is more appropriate to compare numerical differences. The calculated numerical values of the peaks are shown in Table 2. The highest peak intensity is 22 % higher than the as-receive peak intensity at the 6° rake angle value. PBF-LB peak widths are 16 % and 10 % greater than the as-built peak width at −6° and 6° rake angles, respectively. Wrought peak widths are 8 % and 7 % greater than

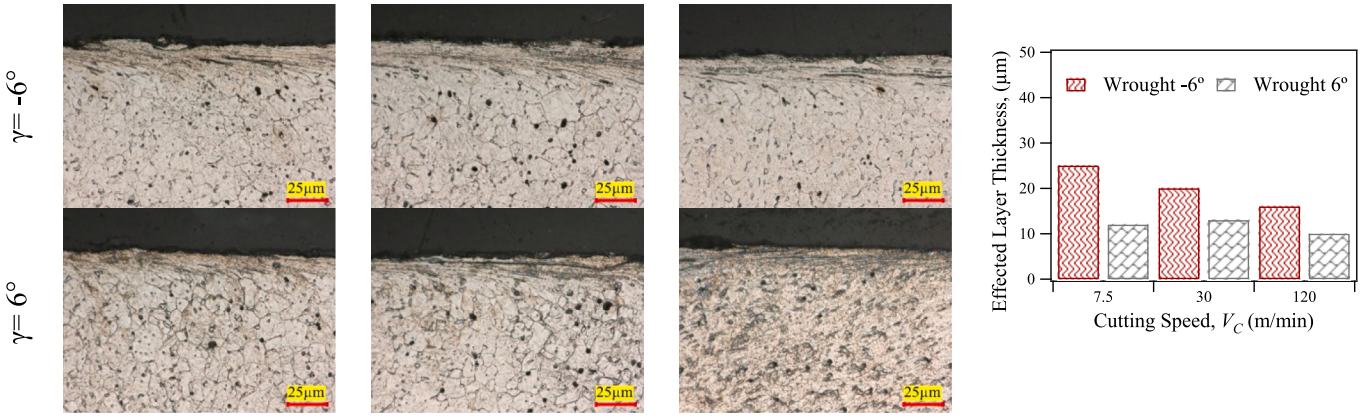

Fig. 16. Wrought material microstructure images and affected layer thicknesses.

Table 2
Calculated peak values.

	Intensity(CPS)	FWHM	2 Theta (°)	Peak Area (CPS*2θ°)
As-built	1185	0.307	43.624	359
PBF-LB -6°	3992	0.358	43.648	1410
PBF-LB 6°	3013	0.338	43.525	1018
As-receive	2058	0.383	43.795	779
Wrought −6°	2476	0.415	43.678	1027
Wrought 6°	2512	0.409	43.557	868

the as-receive peak width at −6° and 6° rake angles, respectively. The numerical ratios show that the amount of grain refinement is higher in the PBF-LB specimen. This shows good agreement with the abrasive behavior described in the previous sections. Also, the effect of machining on specimens can be interpreted with peak patterns. While the PBF-LB peak areas are 292 % and 183 % greater than the as-built, the wrought peak areas are 32 % and 11 % greater than the as-receive at −6 and 6 rake angle values, respectively. It is understood that the machining-induced effect goes deeper in the PBF-LB specimen and is less in the wrought specimen. It is understood from the percentages that the machining-induced effect is higher in the PBF-LB specimens. The machining-induced layer thicknesses in the microstructure images also supports this situation. As-built peak is at the 2θ of 43.624° and as-receive peak is at the 2θ of 43.795°. While wrought peak 2θ angle values decreased, PBF-LB peak 2θ angle values increased at −6° rake angle and decreased at 6° rake angle. The anisotropy behavior of the PBF-LB material caused it to show different peak behavior compared to the wrought material at the same machining parameters.

3.6. Microhardness

Microhardness is an indicator that directly affects the mechanical property characteristics of the material. In particular, it affects the fatigue resistance of parts working in contact with each other [35]. Microhardness values of PBF-LB specimens from the machined surface to a depth of 300 μm are shown in Fig. 19. As-built hardness was reached after 200 μm depth at all cutting speeds. As the cutting speed increased, the hardness values decreased at all rake angles. While the hardness values at negative rake angle values are higher at 7.5 and 30 m/min cutting speeds, it is seen that positive rake angle values are higher at 120 m/min cutting speed. At low cutting speeds, a relatively lower cutting temperature occurs. This contributes to the generation of mechanical energy required for plastic deformation. Due to the low rake angle, a large shear plane area is formed and high cutting forces cause a greater increase in microhardness at negative rake angle values. As the cutting speed increases, the mechanical effect decreases due to the increasing temperature. Therefore, in machining with a negative rake angle at higher cutting speed, the temperature is likely to increase further. The formation of a relatively lower cutting temperature due to the smaller shear plane at the positive rake angle was manifested in the hardness at a cutting speed of 120 m/min. Compared to as-built hardness, the highest and lowest hardness increases were 51 % and 23 % at 7.5 m/min cutting speed, 36 % and 28 % at 30 m/min cutting speed, and 26 % and 21 % at 120 m/min cutting speed, respectively. Due to the anisotropic characteristics of PBF-LB materials, as-built microhardness values may differ in the scan and built planes. This difference is generally between 1 and 3 % [36]. It has also been determined that the hardness values of machined specimens differ at the same rate in the scanned and built planes. Obviously, this difference in hardness between the planes is negligible and there was no significant change after machining. Another expression in terms of anisotropy is the hardness change distance from the machined surface. While the machined specimen hardness reached the as-built hardness at 100–150 μm on the built plane, it reached 100–125 μm on the scan plane. As a matter of fact, error bars both emphasize this situation and serve to express measurement error tolerance.

The comparison of the microhardness values of machined wrought specimens with PBF-LB specimens is shown in Fig. 20. The hardness of both materials decreased with increasing cutting speed. LPBF hardness is higher at a low cutting speed, while wrought hardness is greater at high cutting speed. PBF-LB material is more prone to plastic deformation at low cutting speed. It is seen that the thermal effect increasing at high cutting speed has a greater effect on the plastic deformation behavior of the wrought material. While the anisotropic microstructure of the PBF-LB material changed due to the mechanical effect at low cutting speed, the temperature formed at high cutting speed was not sufficient for the

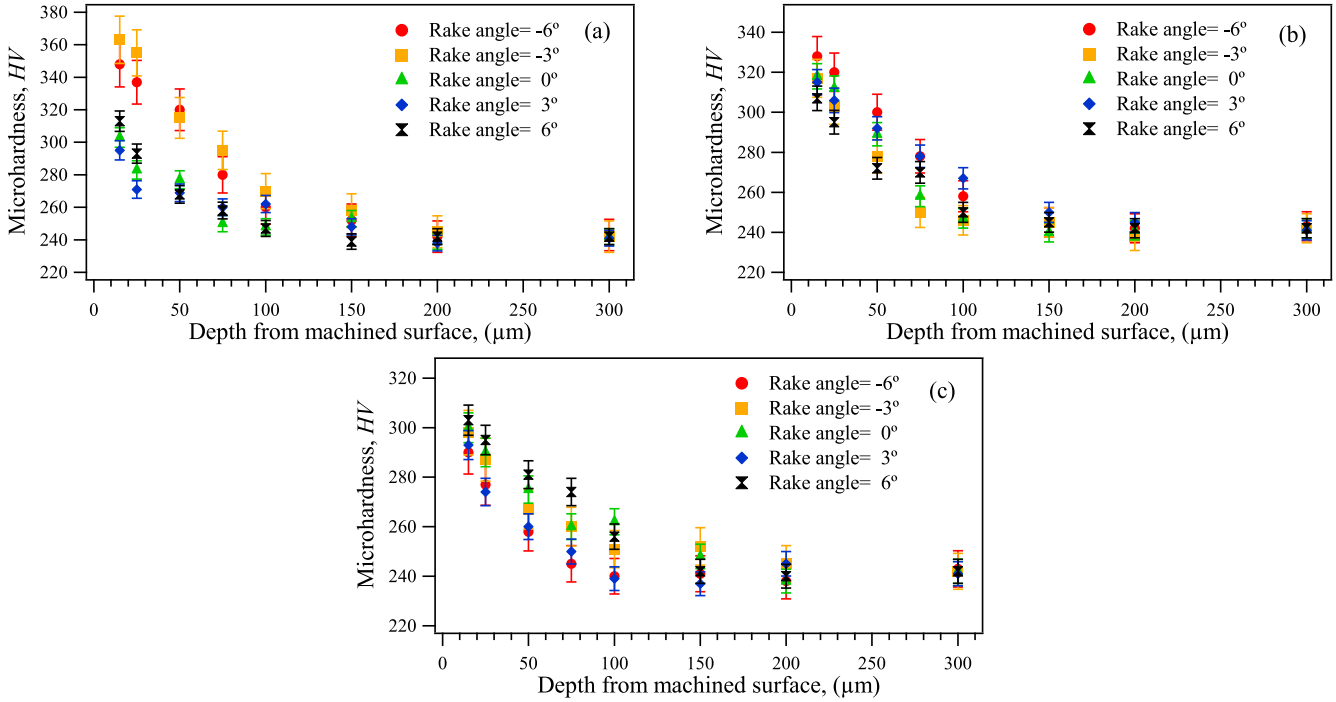

Fig. 19. Measured microhardness values of the machined PBF-LB specimens a)V_c = 7.5 m/min, b)V_c = 30 m/min and c)V_c = 120 m/min.

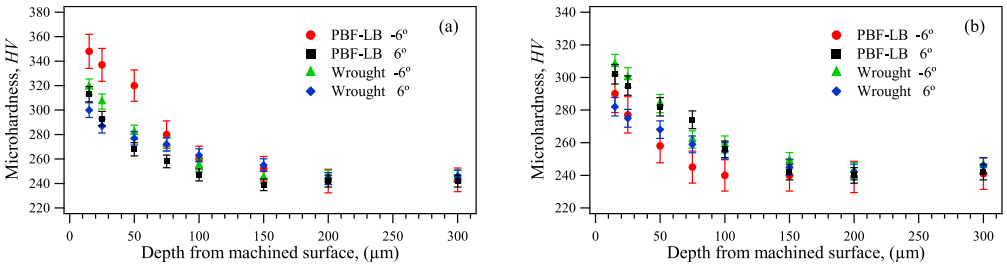

Fig. 20. Measured microhardness values of the machined PBF-LB and wrought specimens a)V_c = 7.5 m/min, b)V_c = 120 m/min.

recrystallization of the material. However, the capacity of plastic deformation of wrought material with equiaxed grain structure at high cutting speed is different from PBF-LB material. As a result, the highest hardness was measured in the PBF-LB specimen with 348 HV at a cutting speed of 7.5 m/min, and the highest hardness was measured in the wrought specimen at a cutting speed of 120 m/min as 308 HV at a rake angle of −6°.

4. Conclusion

In this study, the effect of cutting tool geometry on the machining performance and surface integrity characteristics of PBF-LB and wrought material was investigated and compared. Some important and interesting data from orthogonal cutting experiments are listed below:

- The effect of tool rake angle had a similar effect in terms of cutting force in PBF-LB and wrought material. However, the measured cutting forces are always greater in PBF-LB material at the same cutting parameters.
- The anisotropic characteristic of the PBF-LB material caused the cutting tests to be more abrasive than the wrought, which led to severe wear on the PBF-LB machined cutting tools.
- The machining-induced affected layer thickness is deeper in PBF-LB specimens than wrought specimens. In addition, due to the anisotropic microstructure characteristic, the affected layer thickness in PBF-LB specimens is generally higher in the built plane.
- While the PBF-LB specimen is subjected to more hardening at low cutting speeds than wrought specimens, the hardening ability of wrought specimens is better at high cutting speeds.
- As supported by the microstructure images, XRD results show that grain refinement formation is greater in PBF-LB specimens with anisotropic microstructure than wrought specimen with equiaxed grain microstructure.

The findings obtained from this study are important in terms of showing the difference in machining response, machining-induced surface integrity characteristics, and plastic deformation capacity of 316L stainless steel materials manufactured by the PBF-LB method compared to wrought materials. This study underlines that the same results cannot be obtained due to the different microstructural characteristics of PBF-LB and wrought materials machined in the same parameters. Due to the anisotropic microstructure characteristic created by the PBF-LB method, the built and scan planes of the material does not allow this. In addition, due to the dynamic nature of the machining process, the machining-induced layer thickness of the PBF-LB material is not affected to the same extent on the built and scan planes, making the anisotropy more evident. It also highlights the importance of determining the optimum machining parameters for each material in machining.

Funding

This research did not receive any specific grant from funding agencies in the public, commercial, or not-for-profit sectors.

CRediT authorship contribution statement

Ozhan Kitay: Investigation, Resources, Visualization, Writing – original draft. **Yusuf Kaynak:** Supervision, Validation, Writing – review & editing.

Declaration of competing interest

The authors declare that they have no known competing financial interests or personal relationships that could have appeared to influence the work reported in this paper.

References

[1] Levy A, Miriyev A, Elliott A, Babu SS, Frage N. Additive manufacturing of complex-shaped graded TiC/steel composites. Mater Des 2017;118:198–203.
[2] Du H, Karasev AV, Jönsson PG. Influence of non-metallic inclusions in 316L stainless steels on machining using different cutting speeds. ISIJ International 2021;61:2426–34.
[3] Pradhan S, Singh S, Prakash C, Królczyk G, Pramanik A, Pruncu CI. Investigation of machining characteristics of hard-to-machine Ti-6Al-4V-ELI alloy for biomedical applications. J Mater Res Technol 2019;8:4849–62.
[4] Matos MA, Rocha AMA, Pereira AI. Improving additive manufacturing performance by build orientation optimization. Int J Adv Manuf Technol 2020;107:1993–2005.
[5] Alexander I, Vladimir G, Petr P, Mihail K, Yuriy I, Andrey V. Machining of thin-walled parts produced by additive manufacturing technologies. Procedia CIRP 2016;41:1023–6.
[6] Franco-Correa J, Martínez-Franco E, Alvarado-Orozco J, Cáceres-Díaz L, Espinosa-Arbelaez D, Villada J. Effect of conventional heat treatments on the microstructure and microhardness of IN718 obtained by wrought and additive manufacturing. J Mater Eng Perform 2021;30:7035–45.
[7] Fayazfar H, Salarian M, Rogalsky A, Sarker D, Russo P, Paserin V, et al. A critical review of powder-based additive manufacturing of ferrous alloys: process parameters, microstructure and mechanical properties. Mater Des 2018;144:98–128.
[8] Li Z, Liu X, Wen S, He P, Zhong K, Wei Q, et al. In situ 3D monitoring of geometric signatures in the powder-bed-fusion additive manufacturing process via vision sensing methods. Sensors 2018;18:1180.
[9] Kleszczynski S, Zur Jacobsmühlen J, Sehrt J, Witt G. Error detection in laser beam melting systems by high resolution imaging. In: Proceedings of the twenty third annual international solid freeform fabrication symposium; 2012.
[10] Kaynak Y, Lu T, Jawahir I. Cryogenic machining-induced surface integrity: a review and comparison with dry, MQL, and flood-cooled machining. Machining Science and Technology 2014;18:149–98.
[11] Kong D, Dong C, Ni X, Zhang L, Yao J, Man C, et al. Mechanical properties and corrosion behavior of selective laser melted 316L stainless steel after different heat treatment processes. J Mater Sci Technol 2019;35:1499–507.
[12] Malakizadi A, Mallipeddi D, Dadbakhsh S, M'Saoubi R, Krajnik P. Post-processing of additively manufactured metallic alloys–a review. Int J Mach Tool Manuf 2022;179:103908.
[13] Hoier P, Malakizadi A, Klement U, Krajnik P. Characterization of abrasion-and dissolution-induced tool wear in machining. Wear 2019;426:1548–62.
[14] Malakizadi A, Hajali T, Schulz F, Cedergren S, Ålgårdh J, M'Saoubi R, et al. The role of microstructural characteristics of additively manufactured alloy 718 on tool wear in machining. Int J Mach Tool Manuf 2021;171:103814.
[15] Simmons JC, Chen X, Azizi A, Daeumer MA, Zavalij PY, Zhou G, et al. Influence of processing and microstructure on the local and bulk thermal conductivity of selective laser melted 316L stainless steel. Addit Manuf 2020;32:100996.
[16] Bruschi S, Bertolini R, Bordin A, Medea F, Ghiotti A. Influence of the machining parameters and cooling strategies on the wear behavior of wrought and additive manufactured Ti6Al4V for biomedical applications. Tribology International 2016;102:133–42.
[17] Sartori S, Moro L, Ghiotti A, Bruschi S. On the tool wear mechanisms in dry and cryogenic turning additive manufactured titanium alloys. Tribology International 2017;105:264–73.

[18] Dang J, Cai X, Yu D, An Q, Ming W, Chen M. Effect of material microstructure on tool wear behavior during machining additively manufactured Ti6Al4V. In: Archives of Civil and Mechanical Engineering. 20; 2020. p. 1–15.
[19] Careri F, Umbrello D, Essa K, Attallah MM, Imbrogno S. The effect of the heat treatments on the tool wear of hybrid additive manufacturing of IN718. Wear 2021;470:203617.
[20] Li G, Xu W, Jin X, Liu L, Ding S, Li C. The machinability of stainless steel 316L fabricated by selective laser melting: typical cutting responses, white layer and evolution of chip morphology. J Mater Process Technol 2023;117926.
[21] Kaynak Y, Kitay O. The effect of post-processing operations on surface characteristics of 316L stainless steel produced by selective laser melting. Addit Manuf 2019;26:84–93.
[22] Kaynak Y, Kitay O. Porosity, surface quality, microhardness and microstructure of selective laser melted 316L stainless steel resulting from finish machining. J Manuf Mater Process 2018;2:36.
[23] Souflas T, Bikas H, Ghassempouri M, Salmi A, Atzeni E, Saboori A, et al. A comparative study of dry and cryogenic milling for directed energy deposited IN718 components: effect on process and part quality. Int J Adv Manuf Technol 2022;119:745–58.
[24] Rotella G, Imbrogno S, Candamano S, Umbrello D. Surface integrity of machined additively manufactured Ti alloys. J Mater Process Technol 2018;259:180–5.
[25] Cococcetta N, Jahan MP, Schoop J, Ma J, Pearl D, Hassan M. Post-processing of 3D printed thermoplastic CFRP composites using cryogenic machining. J Manuf Process 2021;68:332–46.
[26] Sun S, Brandt M, Dargusch MS. Characteristics of cutting forces and chip formation in machining of titanium alloys. Int J Mach Tool Manuf 2009;49:561–8.
[27] McGuire MF. Stainless steels for design engineers. Asm International; 2008.
[28] Barkia B, Aubry P, Haghi-Ashtiani P, Auger T, Gosmain L, Schuster F, et al. On the origin of the high tensile strength and ductility of additively manufactured 316L stainless steel: multiscale investigation. J Mater Sci Technol 2020;41:209–18.
[29] Fernandez-Zelaia P, Nguyen V, Zhang H, Kumar A, Melkote SN. The effects of material anisotropy on secondary processing of additively manufactured CoCrMo. Addit Manuf 2019;29:100764.
[30] Ezugwu E. Key improvements in the machining of difficult-to-cut aerospace superalloys. Int J Mach Tool Manuf 2005;45:1353–67.
[31] Manivannan R, Pradeep Kumar M. Improving the machining performance characteristics of the μEDM drilling process by the online cryogenic cooling approach. Materials and Manufacturing Processes 2018;33:390–6.
[32] Bletton O, Duet R, Pedarre P. Influence of oxide nature on the machinability of 316L stainless steels. Wear 1990;139:179–93.
[33] Cui L, Jiang S, Xu J, Peng RL, Mousavian RT, Moverare J. Revealing relationships between microstructure and hardening nature of additively manufactured 316L stainless steel. Mater Des 2021;198:109385.
[34] Zhang X, Chen L, Zhou J, Ren N. Simulation and experimental studies on process parameters, microstructure and mechanical properties of selective laser melting of stainless steel 316L. Journal of the Brazilian Society of Mechanical Sciences and Engineering 2020;42:1–14.
[35] Srinivasan V, Palani P. Surface integrity, fatigue performance and dry sliding wear behaviour of Si3N4–TiN after wire-electro discharge machining. Ceram Int 2020; 46:10734–9.
[36] Palmeri D, Buffa G, Pollara G, Fratini L. The effect of building direction on microstructure and microhardness during selective laser melting of Ti6Al4V titanium alloy. J Mater Eng Perform 2021;30:8725–34.